Characteristics of the fragments produced in central collisions of ^{129}Xe+^{nat}Sn from 32*A* to 50*A* MeV

S. Hudan,[1,*] A. Chbihi,[1] J. D. Frankland,[1] A. Mignon,[1] J. P. Wieleczko,[1] G. Auger,[1] N. Bellaize,[2] B. Borderie,[3] A. Botvina,[1,†] R. Bougault,[2] B. Bouriquet,[1] A. M. Buta,[2] J. Colin,[2] D. Cussol,[2] R. Dayras,[4] D. Durand,[2] E. Galichet,[3,5] D. Guinet,[6] B. Guiot,[1] G. Lanzalone,[3,‡] P. Lautesse,[6] F. Lavaud,[3,§] J. F. Lecolley,[2] R. Legrain,[4,‖] N. Le Neindre,[1] O. Lopez,[2] L. Manduci,[2] J. Marie,[2] L. Nalpas,[4] J. Normand,[2] M. Pârlog,[7] P. Pawłowski,[3] M. Pichon,[2] E. Plagnol,[3] M. F. Rivet,[3] E. Rosato,[8] R. Roy,[9] J.C. Steckmeyer,[2] G. Tăbăcaru,[7] B. Tamain,[2] A. van Lauwe,[2] E. Vient,[2] M. Vigilante,[8] and C. Volant[4]

(INDRA Collaboration)

[1]*GANIL, CEA et IN2P3-CNRS, Boite Postale 5027, F-14076 Caen Cedex, France*
[2]*LPC, IN2P3-CNRS, ENSICAEN et Université, F-14050 Caen Cedex, France*
[3]*Institut de Physique Nucléaire, IN2P3-CNRS, F-91406 Orsay Cedex, France*
[4]*DAPNIA/SPhN, CEA/Saclay, F-91191 Gif sur Yvette, France*
[5]*Conservatoire National des Arts et Métiers, F-75141 Paris Cedex 03, France*
[6]*Institut de Physique Nucléaire, IN2P3-CNRS et Université, F-69622 Villeurbanne, France*
[7]*National Institute for Physics and Nuclear Engineering, RO-76900 Bucharest-Măgurele, Romania*
[8]*Dipartimento di Scienze, Fisiche e Sezione INFN, Università di Napoli "Federico II," I-80126 Napoli, Italy*
[9]*Laboratoire de Physique Nucléaire, Université Laval, Québec, Canada*

(Received 18 November 2002; revised manuscript received 25 February 2002; published 30 June 2003)

Characteristics of the primary fragments produced in central collisions of ^{129}Xe+^{nat}Sn from 32 to 50 *A* MeV have been obtained. By using the correlation technique for the relative velocity between light charged particles (LCP) and fragments, we were able to extract the multiplicities and average kinetic energy of secondary evaporated LCP. We then reconstructed the size and excitation energy of the primary fragments. For each bombarding energy a constant value of the excitation energy per nucleon over the whole range of fragment charge has been found. This value saturates at 3*A* MeV for beam energies 39*A* MeV and above. The corresponding secondary evaporated LCP represent less than 40% of all produced particles and decreases down to 23% for 50 *A*MeV. The experimental characteristics of the primary fragments are compared to the predictions of statistical multifragmentation model (SMM) calculations. Reasonable agreement between the data and the calculation has been found for any given incident energy. However SMM fails to reproduce the trend of the excitation function of the primary fragment excitation energy and the amount of secondary evaporated LCP's.

DOI: 10.1103/PhysRevC.67.064613 PACS number(s): 25.70.Pq

I. INTRODUCTION

Multiple intermediate mass fragment (IMF) production in central heavy-ion collisions is related to the properties of nuclear matter under extreme conditions. Many different models have been proposed in order to explain the observed fragment production, and both theoretically and experimentally the situation is not clear. Models with widely differing basic hypotheses can be equally good at describing the same data such as charge distributions, mean energies, and angular distributions. In order to gain further understanding, it is therefore necessary to have more detailed information on the multifragmentation process.

One aspect of the reactions for which different models give very different predictions are the excitation energies of what we will call from now on the ''primary fragment:'' In other words, the nuclei present around $\sim$100 fm/*c* after the collision, which are not necessarily the same as those arriving in the detectors a few tens of nanosecond later. In quantum molecular dynamics [1–4] simulations or microcanonical metropolis Monte Carlo model (MMMC) [5] calculations, the primary fragments are rather cold, i.e., they are almost unaffected by subsequent secondary decays and arrive unchanged in the detectors. In the former case, the (lack of) excitation energy in the nascent fragments is determined by the collision dynamics, whereas in the latter case, it is an assumption of the model when calculating the statistical weights of the partitions. On the other hand, antisymmetrized molecular dynamics [6–8] and stochastic mean field [9,10] simulations both predict moderately ''hot'' primary fragments in reactions around the Fermi energy, with $E^*_{pr}\sim 2-3A$ MeV [11–13]. Finally, the statistical multifragmentation model (SMM) [14] and the microcanonical multifragmentation model of [15,16] allow primary fragments to be excited, the actual value in any given calculation being determined by energy conservation and the statistical weight given by the associated level density parametrization. This

*Present address: Department of Chemistry, Indiana University, Bloomington, IN 47405.
†On leave from Institute for Nuclear Research, RU-117312 Moscow, Russia.
‡Permanent address: Laboratorio Nazionale del Sud, Via S. Sofia 44, I-95123 Catania, Italy.
§Present address: DAPNIA/SPhN, CEA/Saclay, F-91191 Gif sur Yvette, France.
‖Deceased.

latter may or may not take into account the level density limitation in isolated nuclei at high excitation [17], equivalent to excluding from the primary partitions levels with very short lifetimes or introducing an effective limiting (maximum) temperature for hot nuclei [18,19].

Our previous experimental work [20] has shown that the reconstruction of the average size and excitation energy of the primary fragments is possible by means of intermediate mass fragment-light charged particles (IMF-LCP) relative velocity correlation functions. A constant value of the excitation energy of the primary fragments of about 3*A* MeV has been deduced for the Xe + Sn system at 50 *A* MeV. It was also possible to deduce the multiplicities of the secondary particles evaporated by the primary fragments. More recently, analogous results and conclusions have been obtained for central collisions of Kr + Nb at 45*A* MeV [21]. An important question arises from these studies: What is the evolution of the fragment excitation energies and secondary LCP multiplicities as a function of incident energy? The experimental answer to this question may permit to distinguish between different scenarios and assumptions made by different models. It should give a strong test of the validity of some of their basic hypotheses.

In this paper, we extend the previous study [20] to a wider incident energy range, from 32 to 50 *A* MeV for central collisions of the Xe + Sn system measured with the 4π INDRA detector [22–24]. Excitation functions for the fragment excitation energy and the fraction of secondary emitted LCP correlated to the fragments will be shown. We will give in Sec. II, a brief description of the detector, the way we select the events and an overview of the fragment production. We will describe in Sec. III the method employed to extract the LCP's correlated to each fragment. The method used for the decorrelation in this work is different from the previous one [20] but gives almost the same results. The experimental results are then given in Sec. IV. In Sec. V a comparison of the deduced primary excitation energy and secondary LCP multiplicities to SMM calculations is given. We then discuss the results in Sec. VI.

II. EXPERIMENT

A. Experimental setup

The experiment was performed at GANIL with the multidetector INDRA [22–24]. This charged product detector covers about 90% of the 4π solid angle. The total number of detection cells is 336 arranged according to 17 rings centred on the beam axis. The first ring ($2°-3°$) is made of fast NE102/NE115 phoswich detectors. Rings two to nine cover the angular range from 3° to 45°, and are made of three detector layers: a low pressure gas-ionization chamber, a 300-μm-thick silicon detector, and a 14–10 cm thick CsI(Tl) scintillator. The remaining eight rings cover the angular range from 45° to 176° and have two detection layers: ionization chamber and 7.6–5 cm thick CsI(Tl) scintillators. For the studied system Xe+Sn, fragments with Z up to 54 are identified in the forward region. Beyond 45°, the charge resolution is one unit up to $Z=16$ and few charges above. Over the whole angular range, a very good isotope identification is obtained for $Z=1-3$, except for particles with low energies where ambiguities are unresolved.

The energy calibration of the CsI(Tl) scintillators was obtained for light charged particles (LCP) by means of the elastic and inelastic scatterings of secondary LCP beams ($p,d,t,^3$He, and ^{4}He) produced by the fragmentation of a 95*A* MeV ^{16}O beam on a thick C target. These particles were then momentum selected by the ''alpha magnetic spectrometer'' of GANIL and scattered in a C or Ta target installed in the INDRA reaction chamber. For $Z\geqslant 3$ fragments, the energy calibration was made by using the $\Delta E/E$ technique. A typical energy resolution was about 4%. The energy threshold was a few 100 keV for light particles, 0.7*A* MeV for $Z=3$, and 1.4*A* MeV for $Z=35$. A complete technical description of INDRA, its calibration and its electronics can be found in Refs. [22–27].

B. Selection of central collisions

Two selections have been made to isolate central collisions. The first one is the requirement of quasicomplete events by accepting in the off-line analysis only events having total detected charge (Z_{tot}) $\geqslant$ 80% of the initial total charge of the system. The second is the use of the flow angle (θ_{flow}) selection [28]. This angle is a global observable defined as the angle between the beam axis and the main direction of emission of matter in each event as determined by the energy tensor calculated from fragment ($Z\geqslant 3$) c.m. momenta [29]. It has been shown for heavy-ion reactions in the Fermi energy range [28,30,31] that events with small θ_{flow} are dominated by binary dissipative collisions. On the other hand, events with little or no memory of the entrance channel should be isotropic, thus favoring large θ_{flow} [$P(\theta_{flow}) \sim \sin\theta_{flow}$]. Quasicomplete events having $\theta_{flow}\geqslant 45°$ for 50 *A* MeV bombarding energy and $\theta_{flow}\geqslant 60°$ for the three other systems correspond to an isotropic emission of the IMF in the center of mass of the whole system. These events are compatible with decay of a compact object which could take place after fast emission of a direct light particle component. Indeed, the velocity of the fragments are evenly distributed around the center of mass velocity [32]. By taking into account the detection efficiency and other biases due to the selection, we have estimated the cross sections for ''isotropic central collisions'' to decrease from 115 ± 20 mb at 32*A* MeV to 85 ± 10 mb at 50 *A* MeV. More details about this event selection for Xe+Sn collisions at 32–50 *A* MeV incident energy and the extraction of the cross sections can be found in Ref. [32].

C. Overview of fragment production in central collisions

Before determining the characteristics of the fragments, let us first show an overview of their production in central collisions of Xe + Sn from 32 to 50 *A* MeV. Figure 1 shows their charge distributions normalized to the number of events so that the four bombarding energies can be compared. The production of small fragments ($Z\leqslant 10$) increases with incident energy. For the charge range from 10 to 15, the four distributions exhibit a kind of ''plateau.'' In this range, the

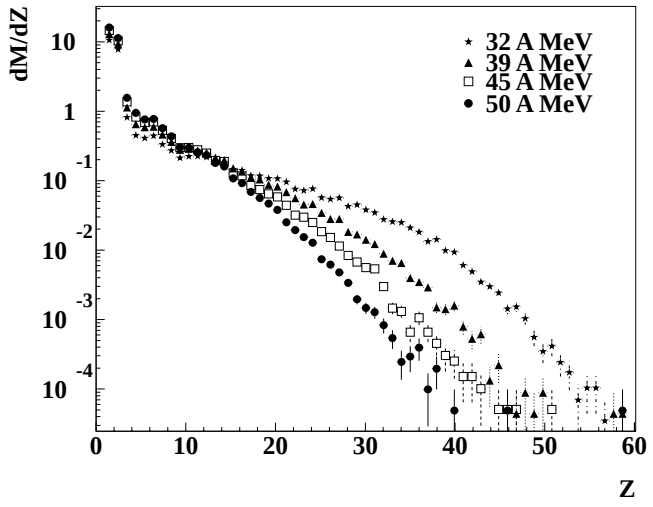

FIG. 1. Charge distributions of fragments produced in central collisions of Xe + Sn at four incident energies: 32, 39, 45, and 50 *A* MeV.

fragment production rates are roughly equivalent whatever the incident energy is. Finally, the charge distributions evolve from a broad shape at lower incident energy, where residues up to the size of the projectile are observed, toward an almost exponential form at 50*A* MeV, favoring the production of lighter fragments. Moreover Fig. 2, where the distributions of the heaviest fragment in the event are shown, confirms this behavior. Here, again the distribution at 32*A* MeV is very broad, its average value is $\langle Z_{max} \rangle = 25$, it decreases to smaller $\langle Z_{max} \rangle = 15$ at 50*A* MeV. It is important to notice that, even with this strong evolution in the charge distribution, the mean fragment multiplicity does not change too much with the incident energy. It evolves from five to seven fragments with $Z \geqslant 3$ only.

Concerning the kinematic characteristics of the fragments, Fig. 3 shows an example of the fragment angle-integrated

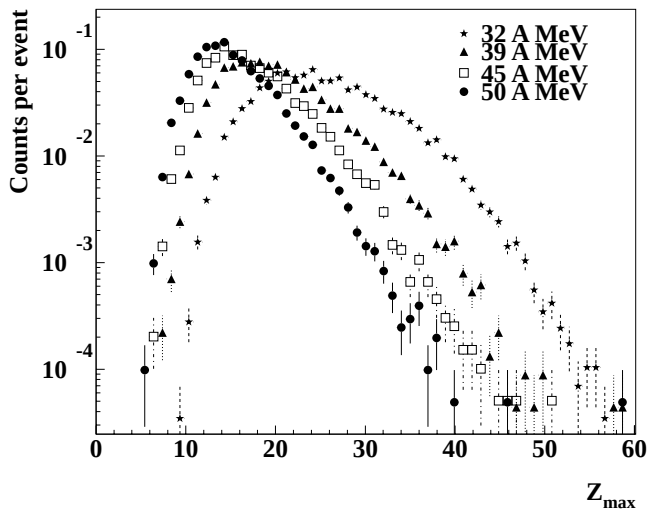

FIG. 2. Charge distributions of the heaviest fragment per event produced in central collisions of Xe+Sn at four incident energies: 32, 39, 45, and 50 *A* MeV.

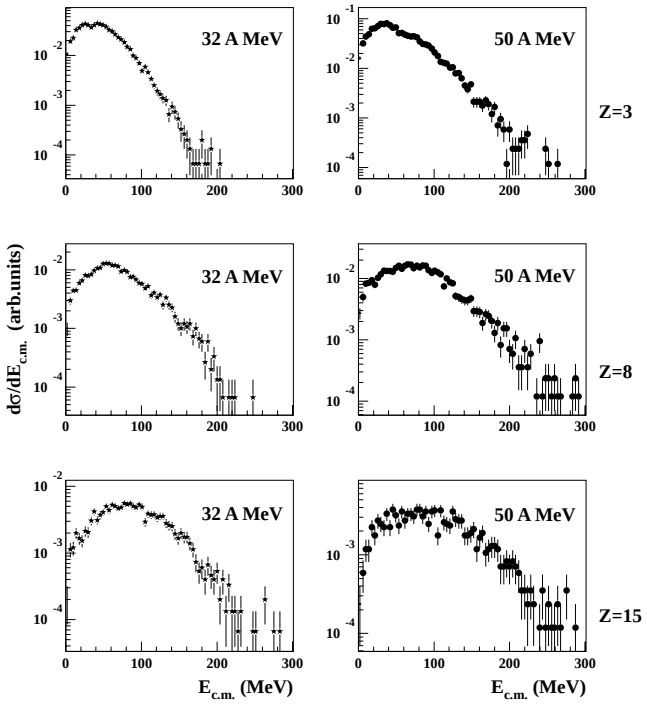

FIG. 3. Angle-integrated center of mass kinetic energy spectra of Li, O, and P produced in central collisions of Xe+Sn at 32 and 50 *A* MeV.

center of mass kinetic energy spectra for Li, O, and P nuclei produced in central collisions of Xe+Sn at 32 and 50 *A* MeV. The distributions are broad; they are broader for the heavier elements. Comparing the spectra obtained at 32 and 50 *A* MeV, we observe easily that their shape, particularly the slopes of their exponential tails, are different. The distributions are broader and harder at 50*A* MeV than at 32*A* MeV.

We finally present in Fig. 4, for the four incident energies,

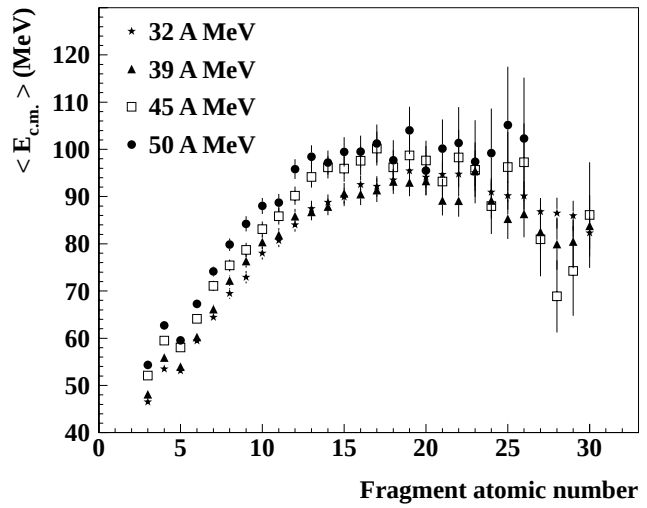

FIG. 4. Mean center of mass kinetic energy of the fragments produced in central collisions (θ_{flow} selection, see text) of Xe +Sn at four incident energies: 32, 39, 45, and 50 *A* MeV as a function of their atomic number. The statistical error bars are shown.

the mean center of mass kinetic energy of the fragments as a function of their atomic number. It increases with the charge Z and then saturates beyond $Z=15$. It also increases with the bombarding energy but very little. We wondered whether this observation is true for central collisions in general, or is rather dependent on our selection. In fact, it is the mean kinetic energy of the heaviest fragment which ''saturates,'' while that of the other fragments increases monotonously with Z. The θ_{flow} selection we use is derived from fragment kinetic properties and, therefore, its effect on observables such as fragment energies and angular distributions must be taken into account in events selected in this way. Nevertheless, this selection has little influence on the study of individual fragment characteristics such as excitation energy and secondary decay, whatever the mechanism of their formation.

III. EXTRACTION OF SECONDARY EVAPORATED LIGHT CHARGED PARTICLES

The main aim of this work is to extract the intrinsic properties of the fragments independently of the mechanism responsible for their formation. Are they excited? If so what are the associated LCP evaporated from the parents? Reconstructing the primary fragments assumes that we are able experimentally to isolate the secondary contribution. This is possible if the fragments formed are not too excited, so that the time scale associated with their decay is much greater than the time scale of their production. The origin of the fragments is still an open question but is not the subject of this paper.

A. Correlation functions

In the preceding section, it was shown that on average, about six fragments are produced in central collisions of Xe+Sn at different energies. However, the production of LCP is much more important; on average, their number reaches 28 particles for the 50A MeV beam energy. There are at least three different stages to produce these particles: (i) in the early stage of the collision, in this case, we call them primary particles; (ii) at the same time as the formation of the fragments; (iii) they can be emitted from the excited primary fragments, we call those the secondary particles. Correlation functions are a powerful tool for extracting small signals. This is the method we used to extract, on the average, the LCP emitted from each fragment. With the help of simulations, we have developed a correlation technique to extract possible signals [11,20,33].

Figure 5 shows the relative velocity distributions: (i) for P-α pairs taken from the same events, (ii) for the uncorrelated events obtained by taking the fragment from a given event and the light particle from another event, (iii) for the correlation function defined as the ratio of the correlated and uncorrelated relative velocity distributions, (iv) for the difference correlation function defined as the difference between the correlated and uncorrelated distributions. In this work to decorrelate the relative velocity between the fragment and the LCP pairs, we used the event mixing procedure [34]. In this example, for each phosphorus found in an event

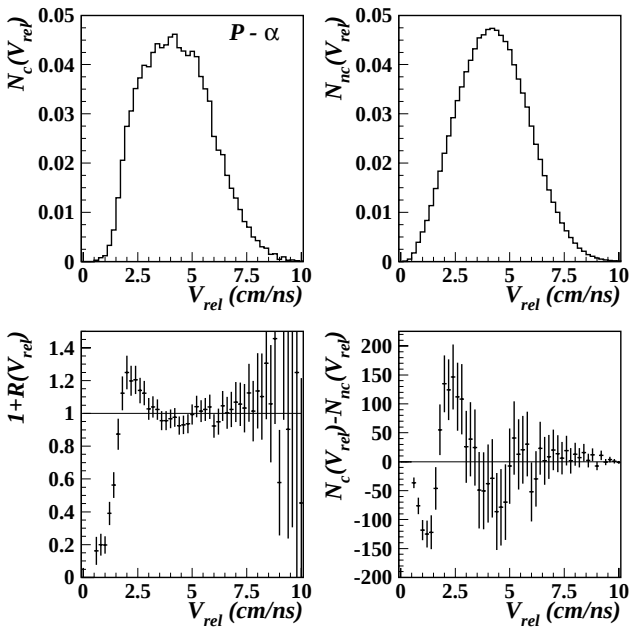

FIG. 5. Relative velocity spectra of P-α pairs observed for the Xe+Sn system at 32A MeV. Top-left hand panel corresponds to the correlated events, top-right hand panel corresponds to the uncorrelated events (mixed events), bottom-left hand panel corresponds to the correlation function, and bottom-right panel shows the difference function.

having a number of α's N_a we take randomly N_a α's emitted in N_a other events.

This technique is different from the one reported in Ref. [20], where Li nuclei were used to decorrelate the events. The problem with such a technique is that the Li can be the product of the known resonance of ^{7}Be which decays to ^{6}Li+p and increases the background, thus decreasing the yield of true correlated protons. However, the final result is almost the same (within the error bars) as the old method of decorrelation of events based on Li.

As we can see, the example presented in Fig. 5, exhibits a bump around 2.5 cm/ns relative velocity in the correlation function and difference function that may be related to the evaporation of an α particle from a parent of phosphorus. The behavior of this correlation encourages us to make such an analysis. However, it is necessary to simulate the background in order to extract the signal.

B. Simulation of the background shape

The objective of this simulation is not to reproduce the data, it is more to have an idea about the shape of the background. We used a modified version of the SIMON event generator [35] to simulate a scenario deduced from Boltzmann-Nordheim-Vlasov [36] calculations. Two steps are assumed in these simulations. The first step is the cooling of the initial fused system through a sequential light particles (LP) emission process (primary LP), the second is the fragmentation of the smaller remaining source where the remaining excitation energy is shared between a fixed number of primary fragments (typically from six to seven fragments).

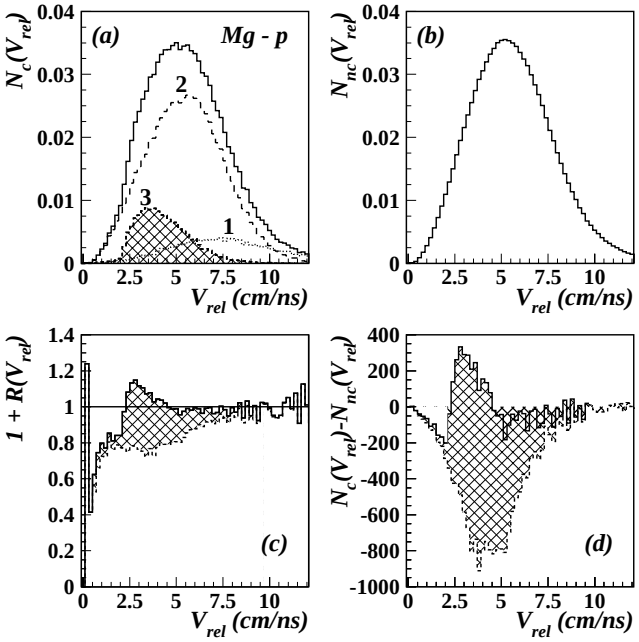

FIG. 6. Relative velocity spectra of Mg-p pairs simulated for the Xe+Sn system at 32*A* MeV. (a) For correlated events: total spectrum (thick histogram), contribution of primary emission ($a1$, dotted histograms, high energy contribution), secondary emission from primary fragments which produce Mg nuclei ($a3$, hatched-dashed) and do not produce the considered fragment ($a2$, dashed histograms). (b) For uncorrelated events. (c) The correlation function (continuous histogram), the real background (dashed histogram) and the contribution from the secondary emission from the parents of the Mg fragments (hatched area) are shown. (d) The difference function is shown here. The notations are similar to (c).

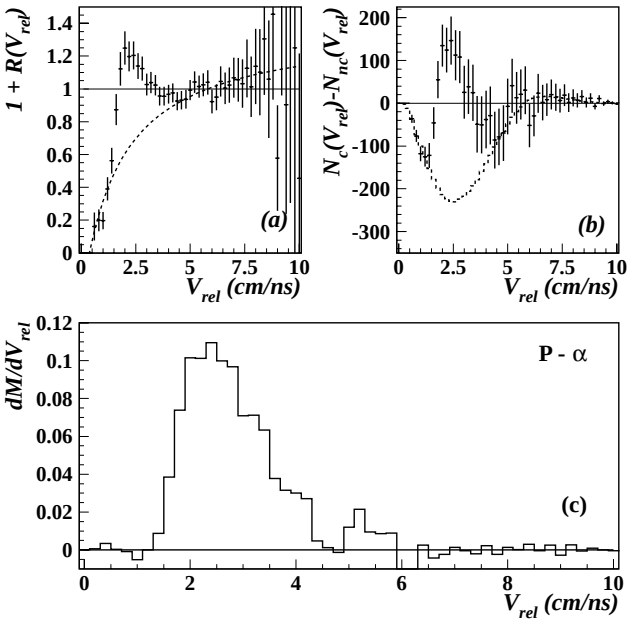

FIG. 7. P-α correlation measured in central collisions of Xe + Sn at 32*A* MeV. (a) correlation function. (b) difference function. (c) velocity spectrum of α's in the center of mass of the phosphorus fragment, obtained from the subtraction of the difference function [data point in (b)] and the background [dashed line in (b)].

Then the primary fragments decay sequentially while moving apart under Coulomb forces plus an initial radial velocity. This simulation reproduces reasonably well the global experimental features. In particular, the kinematic observables are well reproduced (see, for example, Ref. [30]).

The calculated relative velocities are shown in Fig. 6(a) (thick lines) for Mg-*p* pairs for simulations carried out with input parameters which reproduce data for the 32*A* MeV Xe + Sn central collisions. Since in this version of SIMON, we know which particle is emitted from which fragment, we plotted in the same figure the different contributions: the primary contribution (dotted histogram) that we call contribution 1, the evaporated protons from all other fragments except the parents of magnesium (dashed histogram) that we call contribution 2 and finally, the protons emitted from the parents of detected magnesium fragments (hatched-dashed histogram) called contribution 3. As expected, the latter contribution is very small, it represents the protons truly correlated to the magnesium nucleus that we must extract from the data. Figure 6(b) shows the uncorrelated relative velocity for Mg-*p* pairs reconstructed by mixing the calculated events. Figures 6(c) and 6(d) show the Mg-*p* correlation function [the ratio of the correlated and uncorrelated relative velocity distributions of Figs. 6(a) and 6(b)] and the difference function (the difference of the latter distributions), respectively. In the same figures are plotted the associated true backgrounds (dashed histograms) calculated by dividing (subtracting) the sum of contributions 1 and 2 by the uncorrelated distribution [of Fig. 6(b)]. The hatched areas represent the contribution of secondary emission from the parents of magnesium (contribution 3). The shape of the background shown in Fig. 6(c) is well fitted by the function:

$$R(V_{rel}) = A - \frac{1}{BV_{rel} + C}, \tag{1}$$

where *A*, *B*, and *C* are parameters which differ for each fragment-LCP pair. In fact only three coordinates are needed to solve this equation, we then used particular points from Fig. 6(d) to do so. The first one corresponds to the first point at which the difference function is equal to zero (at small relative velocity). The second point used is the local minimum seen at small relative velocity (around 2.5 cm/ns) in the difference function [Fig. 6(d)] which corresponds to the minimum relative velocity allowed by the Coulomb barrier. The third one corresponds to the first point, where the difference function is equal to zero just after the second minimum, in this region the secondary evaporation vanishes.

In order to validate the method employed to estimate the background, several tests have been made. We summarize the following two most important tests that we already reported in Ref. [30]:

(a) We compared the number of protons deduced by subtracting from the difference function [Fig. 6(d)] the real background and the background evaluated by the parametrization of Eq. (1). We recover 91% of the evaporated protons

from Mg and 84% of evaporated protons from all prefragments.

(b) The second check is related to the possible upper limit of the method. We performed SIMON simulations assuming higher excitation energies in the primary fragments. For 7.5*A* MeV excitation energies, we recovered 81% of evaporated protons. This result indicates that the fraction of all evaporated protons recovered by this method is rather insensitive to the excitation energies of the primary fragments.

Since the experimental shape of the correlation function as well as the difference function (Fig. 5) have the same behavior as those in our simulation, we applied the same method to the experimental data to remove the background. From this simulation and method developed above, we are able to isolate the LCP evaporated by the primary fragments.

C. Application to the data

Figure 7 shows the experimental correlation function, the difference function, and the velocity distribution of α correlated to phosphorus fragments for the central collisions of Xe+ Sn at 32*A* MeV. In the same figure are plotted the corresponding background calculated with Eq. (1) by using three points taken from the experimental distributions as described in the above section. Therefore, the α velocity spectrum is deduced by subtracting the background (the curve in Fig. 7, upper right panel) from the difference function. This contribution represents the spectrum of α particles emitted by the parent of *P* fragment. From the mean value of the distribution we can deduce the average kinetic energy of α. Its integral normalized to the total number of phosphorus nuclei provides the average multiplicity of α particles evaporated from parents of *P* fragments.

The uncertainties of the extracted quantities are mainly related to the uncertainty of taking the three points which define the background. In practice, the first minimum in the difference function is easy to locate: the corresponding error is small [see Fig. 7(b)]. The two other points are more difficult to extract, with the possibility of significant uncertainties. We then decided to take intervals around each point which are divided into a number of bins. Considering all possible combinations of one bin in the first interval and another in the second leads to a distribution of multiplicities. This distribution has a narrow Gaussian shape. We then consider the mean value of this distribution as the average multiplicity and its half-width as the error due to the method. An alternative method would be to use the analytic background function, Eq. (1) determined from simulations, in addition to a Maxwellian evaporation spectrum, in order to perform a global fit to the entire correlation function. In this way, background and ''signal'' parameters would be determined along with their estimated errors by the fitting procedure, as well as a χ^2 value allowing to evaluate the validity of the method. This approach would be preferable in the future in order to extend the analysis to a wider range of data.

IV. EXPERIMENTAL RESULTS

A. Average multiplicities and kinetic energies of the LCP correlated to the fragments

We applied the method described above for all fragment-LCP pairs made by combining LCP isotopes (p,d,t, ^{3}He, and α) and a range of fragments emitted in central collisions between Xe and Sn at four incident energies 32, 39, 45, and 50 *A* MeV. However, due to a small cross section for heavy fragment production which implies a low statistics (see Figs. 1 and 2), we performed these analyses for a limited range of fragment charges depending on the beam energy. Thus the maximum fragment charge we studied at 32*A* MeV was 30, 27 at 39*A* MeV, 22 at 45*A* MeV and 20 for 50 *A* MeV.

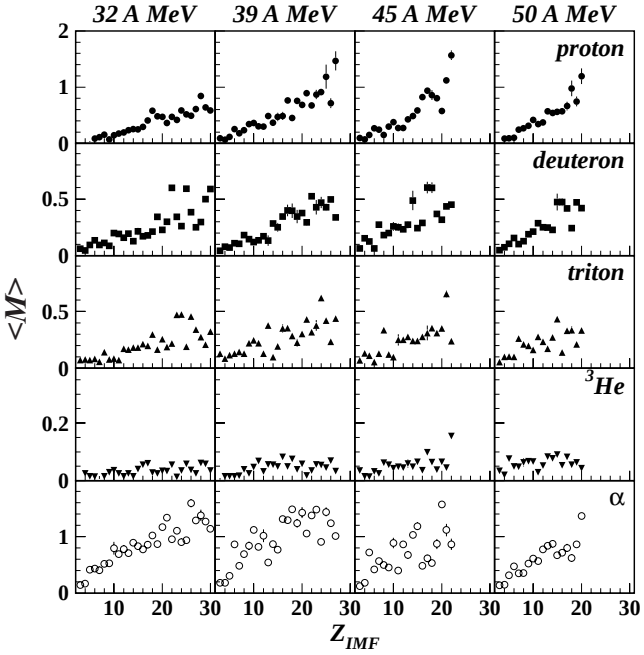

FIG. 8. Average secondary multiplicities per fragment of the evaporated p,d,t, ^{3}He, and α particles as a function of the atomic number of the fragments for central collisions of Xe+ Sn at 32, 39, 45, and 50 *A* MeV. The error bars correspond to the error due to the background extraction method.

The extracted average LCP multiplicities and their average kinetic energy are given in Figs. 8 and 9 as a function of the charge Z_{IMF} of the detected fragments and for the four bombarding energies. The average multiplicities increase with the fragment size. The multiplicities are low and do not exceed a value of 1.5 which implies that the excitation energy of the corresponding primary fragments is moderate. For a given light charged particle, the multiplicity seems not to change with the beam energy. From the spectra of the LCP evaporated from the parents of the detected fragments, we can extract the mean kinetic energy. This is shown in Fig. 9. It increases slightly with the charge of the fragment for the four incident energies and in particular for proton and α particles. Notice that the kinetic energies of ^{3}He are high compared to the values of the other particles. The observed effect may be due to the higher identification threshold energy for ^{3}He.

B. Reconstruction of the size and excitation energy of the primary fragments

To reconstruct the charge of the primary fragments, we used the LCP multiplicities correlated to each fragment as

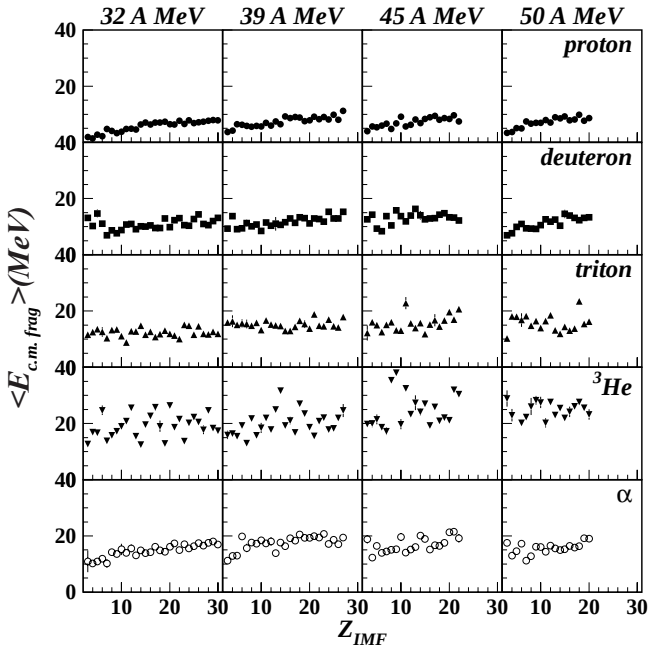

FIG. 9. Fragment center of mass average kinetic energy of the secondary evaporated p,d,t, ^{3}He, and α particles as a function of the atomic number of the fragments for central collisions of Xe + Sn at 32, 39, 45, and 50 A MeV.

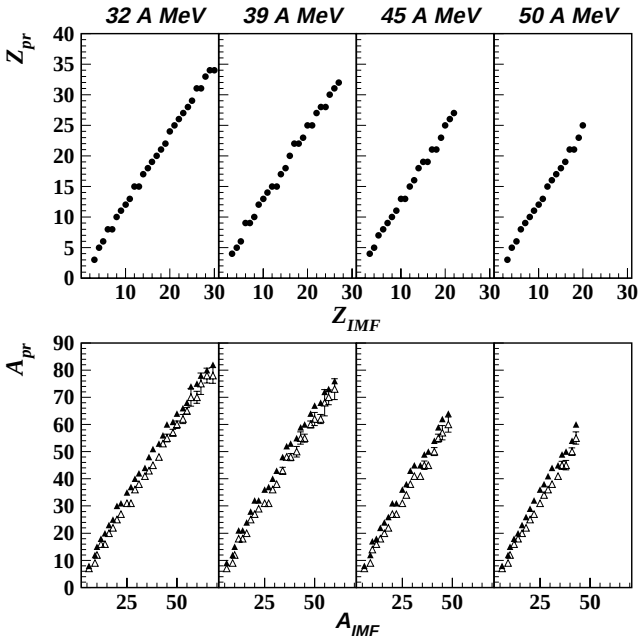

FIG. 10. The reconstructed charge and mass of the primary fragments as a function of the atomic number/mass of the detected fragments for central collisions of Xe+Sn at 32, 39, 45, and 50 A MeV. Two assumptions to reconstruct the masses are given: the open triangles correspond to the valley of stability case and the black triangles represent the N/Z conservation hypothesis (see text).

described in the last paragraph. Therefore, the average charge of the primary fragment, $\langle Z_{pr}\rangle$, is given by the sum of the detected fragment and all evaporated LCP's charge weighted by their corresponding multiplicities. $\langle Z_{pr}\rangle$ is then given by the relationship

$$\langle Z_{pr}\rangle = Z_{IMF} + \sum z_i \langle M_i\rangle, \tag{2}$$

where Z_{IMF} is the detected fragment charge, z_i and $\langle M_i\rangle$ are the charge and the average multiplicity of the evaporated particle $i=p,d,t,^3$He, and α.

In order to reconstruct the mass of the primary fragments, a quantity needed to deduce the excitation energy, we made two extreme assumptions: the first one is that the primary fragments are produced in the valley of stability, the second assumes that they are produced with the same N/Z ratio as the composite initial system (N/Z conservation assumption). However, as mentioned above the INDRA detector does not resolve the fragment isotopes, we, therefore, made an additional assumption that supposes that the Z-identified detected fragments have a mass corresponding to their valley of stability isotope. We used the same expression as in Ref. [20] which approximates the valley of stability. In the framework of these assumptions, we deduce from the primary fragment masses the number of neutrons evaporated from the primary fragments.

Figures 10 and 11 show the result of this reconstruction for the four incident energies. The values of the primary charge (Fig. 10, upper panel) obtained vary from 1 to 5 charge units larger than the detected fragment. The mass of the primary fragment depends on the assumption (Fig. 10,

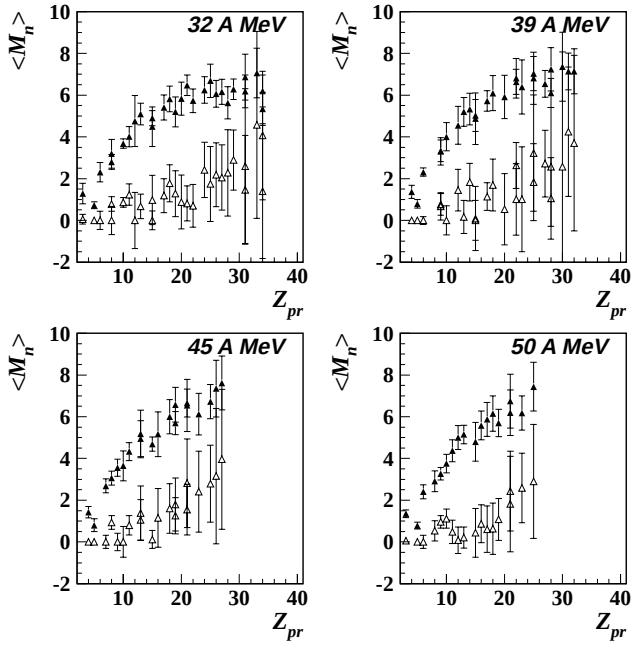

FIG. 11. The average neutron multiplicities evaporated from the primary fragments deduced for central collisions of Xe+Sn at 32, 39, 45, and 50 A MeV. Two assumptions to reconstruct the mass are given: the open triangles correspond to the valley of stability case the black triangles represent the N/Z conservation hypothesis (see text).

down panel). The average neutron multiplicities are deduced from the mass conservation, knowing the mass of the primary fragment, the detected fragment and the mass of the secondary light charged particle contribution. Figure 11 shows for the two assumptions the evolution of the number of neutrons for the four systems as a function of the deduced primary fragment atomic number. Whatever the beam energy, the multiplicity of neutrons reaches quite high values, up to seven neutrons for the N/Z ratio conservation assumption. This is due to our assumption that detected fragments have their valley of stability mass. Clearly, when we also assume that the primary fragments are produced in the valley of stability, the deduced neutron multiplicity cannot be very high. Conversely, imposing an N/Z of 1.39 for nuclei with $Z=3-30$ means that primary fragments have large neutron excess compared to the (valley of stability) detected fragments.

At this stage, the calorimetric procedure can be applied to reconstruct the average excitation energy of the primary fragments ($\langle E^*_{pr}\rangle$). It is given by the relationship

$$\langle E^*_{pr}\rangle = \sum \langle M_{LCP}\rangle\langle E_{LCP}\rangle + \langle M_n\rangle\langle E_n\rangle - Q, \qquad (3)$$

where $\langle E_{LCP}\rangle$ and $\langle E_n\rangle$ are the average kinetic energies in the frame of the source (fragment) of the measured evaporated LCP's and the deduced neutrons with the average multiplicity $\langle M_n\rangle$. The neutron kinetic energy $\langle E_n\rangle$ is taken as the proton kinetic energy minus the proton Coulomb barrier. Q is the mass balance of the reaction.

Figures 12 shows the result of this procedure for the two scenarios and at the four bombarding energies. As expected from the deduced multiplicities (see Sec. IV A), the excitation energy in MeV increases with the size of the primary fragment for all bombarding energies and for the two assumptions (Fig. 12). However, for the 32A MeV system, $\langle E^*_{pr}\rangle$ seems to saturate for the heavier fragments. We could wonder if this is due to limitations of the method. However, as we already mentioned in Sec. III B, simulations have been performed at much higher excitation energy into the primary fragments showing that we recover more than 80% of the evaporated protons.

We also tried an alternative assumption for the final masses of the detected fragments which supposes that they follow the evaporation attractor line (EAL) described by Charity [37]. Keeping the two hypotheses made for the mass of the primary fragments, we reconstructed their excitation energies using the EAL assumption. Compared to our first assumption of valley-of-stability masses for the final cold fragments, the EAL assumption does not modify the excitation energy of primary fragments except for the data at 32A MeV bombarding energy. This is shown in Fig. 12 (open circles in the upper left panel). Here, for the largest primary fragments ($Z>20$), we observe a small increase of $\langle E^*_{pr}\rangle$ compared to the previous assumption.

To decide between the scenarios for primary fragment mass, valley of stability or with the N/Z conservation assumption, extensive statistical calculations have been performed using the GEMINI [38] code, for the 50A MeV system.

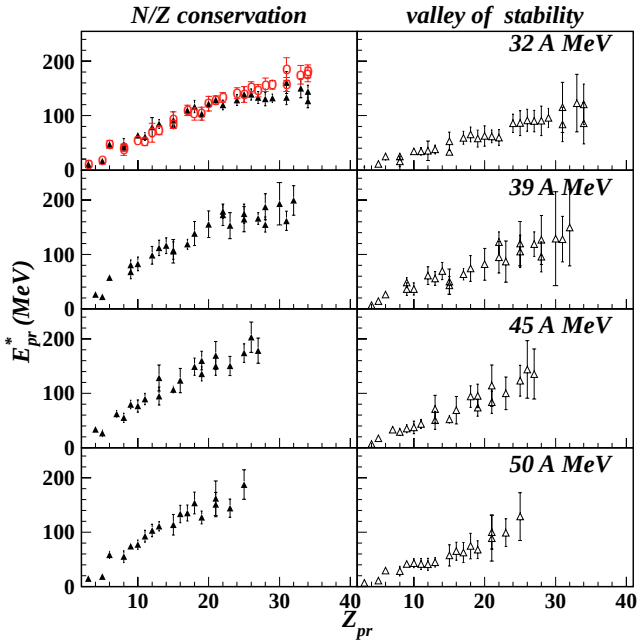

FIG. 12. Average excitation energy of the primary fragments as a function of their atomic number for the central collisions of Xe + Sn at 32, 39, 45, and 50 A MeV. Left panels: the primary fragments have the same N/Z as the combined system. Right panels: the primary fragments are produced in the valley of stability. The masses of detected fragments are assumed to follow the valley of stability except for the data points represented by open circles where the EAL assumption is used (see text).

In these calculations, the input to the code was the experimental deduced primary charge, the fragment masses with the two assumptions, and the associated excitation energies. The comparison to the experimental LCP multiplicities and kinetic energies suggests that the N/Z conservation assumption is the most reasonable scenario. Details of these calculations are given in Ref. [20].

The linear trend of the $\langle E^*_{pr}\rangle$ with the primary charge indicates that the average excitation energy per nucleon $\langle e^*_{pr}\rangle$ is constant whatever the size of the primary fragment. In Fig. 13, we verified the latter characteristic by plotting this variable. The horizontal lines in this figure represent a good fit to the whole set of average excitation energies with a constant global value for all fragments for each bombarding energy. Except for the very smallest ($Z_{pr}<5$) primary fragments, the data points lie on this straight horizontal line within error bars. For the 32A MeV bombarding energy, the extracted $\langle e^*_{pr}\rangle$ using the EAL assumption (open circles in the upper left panel of Fig. 13) appear to be in better agreement with a constant value for all Z_{pr} than those obtained with assumption of valley-of-stability detected masses (solid triangles in the upper left panel of Fig. 13).

Figure 14 shows the evolution of the fitted average excitation energy of primary fragments as a function of the bombarding energy. The vertical bars are the standard deviations from the mean values. They are small and do not exceed 1A MeV, which supports the constancy of the value of $\langle e^*_{pr}\rangle$. For the N/Z conservation assumption, the excitation energy

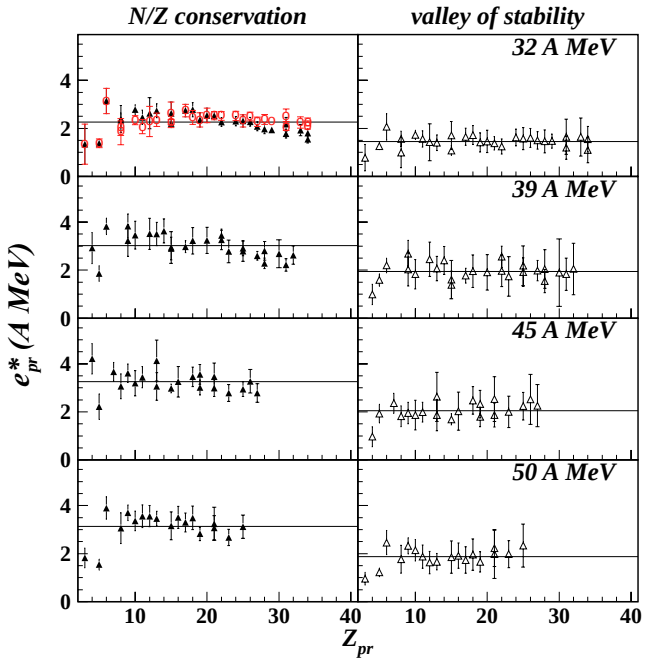

FIG. 13. Average excitation energy per nucleon of the primary fragments as a function of their atomic number for the central collisions of Xe+Sn at 32, 39, 45, and 50 *A* MeV. The horizontal lines represent a fit to the average excitation energies with a Z_{pr}-independent value for each bombarding energy. Left panels: the primary fragments have the same N/Z as the combined system. Right panels: the fragments are produced in the valley of stability. The vertical bars indicate errors due to the method. The masses of detected fragments are assumed to follow the valley of stability except for the data points represented by open circles where the EAL assumption is used (see text).

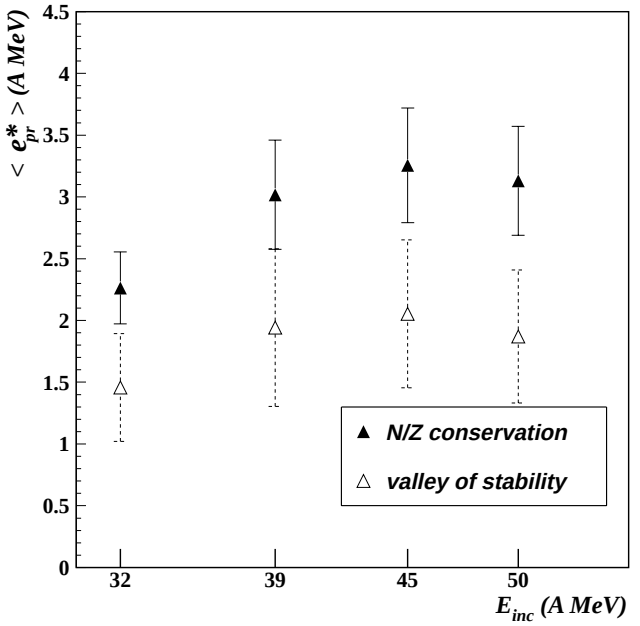

FIG. 14. Average excitation energy per nucleon of the primary fragments as a function of bombarding energy. The black and open triangles correspond to the primary fragments having the same N/Z as the combined system, and produced in the valley of stability, respectively. The error bars correspond to the standard deviation from the mean values.

per nucleon increases from 2.2*A* MeV (2.3*A* MeV for the EAL assumption case) at 32*A* MeV and saturates at 3*A* MeV beyond 39*A* MeV. For the valley of stability assumption, $\langle e^*_{pr} \rangle$ saturates also but at a lower value.

The constancy of the fragment excitation energy per nucleon, $\langle e^*_{pr} \rangle$ for different fragment masses, seen in Fig. 13 has been interpreted in Ref. [20] as meaning that, on the average, thermodynamical equilibrium was achieved at the disassembly stage of the system. Only one bombarding energy (50 *A* MeV) was available in the previous work. On the other hand, the saturation of $\langle e^*_{pr} \rangle$ beyond 39*A* MeV beam energy (Fig. 14) may indicate that the fragments reach their excitation energy limit (or limiting temperature) [18,19].

C. Proportion of the evaporated light charged particles

In Sec. IV A we have extracted the average multiplicities of the secondary evaporated light charged particles for a given fragment. It is interesting to use this information in order to study the characteristics of the multifragmentation events. Indeed, the LCP multiplicity per event can be another pertinent observable. Table I shows the secondary LCP multiplicities per event, the total LCP measured per event, and the ratio of both quantities, for the four beam energies. The secondary LCP multiplicities per event are defined as the sum of the secondary evaporated LCP's per fragment, extracted by the method described above, weighted by the measured fragment multiplicity per event M_{IMF}. These values are plotted in Fig. 15 as a function of the beam energy.

The fraction of helium isotopes evaporated in the decay of the primary fragments is higher than for those of hydrogen. This difference is more pronounced at lower beam energy. We observe also that the maximum proportion of evaporated particles does not exceed on the average 35% of the total number of produced light charged particles. The proportion of secondary particles increases between 32 and 39 *A* MeV, which reflects the increasing of the excitation energy of the primary fragments as it is seen in Fig. 14. Then this fraction decreases for higher incident energies, it reaches 23% at 50 *A* MeV, while $\langle e^*_{pr} \rangle$ saturates.

It should be noticed that the proportion of the secondary evaporated particles given is a lower limit, because we did not consider the contribution that can originate from the decay of unstable nuclei [39] such as ^{8}Be, ^{5}Li etc., and the decay of short-lived excited sates. We, finally, have to stress that the results we obtained with the method described above are given on the average.

V. COMPARISON WITH A STATISTICAL MODEL

An application of the experimental estimation of this secondary statistical component is to constrain the statistical multifragmentation models [5,14–16,40–42]. The comparison of the extracted quantities with these models provides a

TABLE I. Xe+Sn, central collisions: mean multiplicities of evaporated particles per event. For each energy and particle, $M_{ev.}$ is the multiplicity of evaporated particles, M_{tot} the total multiplicity, and $M_{ev.}/M_{tot}$ the percentage of evaporated particles.

$E_{inc.}$		^{1}H	^{2}H	^{3}H	^{3}He	^{4}He	$Z=1$	$Z=2$	$Z=1$ and 2
32	$M_{ev.}$	0.97	0.83	0.71	0.12	3.09	2.51	3.21	5.72
	M_{tot}	5.98	2.85	1.84	0.38	7.36	10.67	7.88	18.55
	$P_{ev.}$ (%)	16.22	29.12	38.59	31.58	41.98	23.52	40.74	30.84
39	$M_{ev.}$	1.73	0.92	1.1	0.18	4	3.75	4.18	7.93
	M_{tot}	7.16	3.3	2.45	0.55	8.6	12.91	9.15	22.06
	$P_{ev.}$ (%)	24.22	27.95	44.69	32.36	46.49	29.06	45.64	35.94
45	$M_{ev.}$	1.68	1.21	1.01	0.24	3.2	3.91	3.44	7.35
	M_{tot}	7.82	3.85	2.93	0.72	9.39	14.6	10.11	24.71
	$P_{ev.}$ (%)	21.48	31.51	34.61	33.89	34.04	26.76	34.03	29.73
50	$M_{ev.}$	1.42	0.98	1.01	0.34	2.6	3.41	2.94	6.34
	M_{tot}	8.37	4.35	3.3	0.89	10.1	16.02	10.99	27.01
	$P_{ev.}$ (%)	16.99	22.51	30.45	37.98	25.71	21.26	26.71	23.48

crucial test of some of their basic assumptions. Since in the MMMC [5] model, the primary fragments undergo instantaneous decay with neutron emission only, it cannot be used for comparison with the data.

We have chosen to compare our data, with more details, to the SMM model using input source parameters very close to the ones already optimized in previous works [32,43,44]. As shown there, SMM provides a very good description of experimental fragment partitions. In the present paper, we aim to analyze the general behavior of excitation energy of primary fragments, therefore, for simplicity, the size of the initial source has been fixed to be $Z=83$ and $A=198$ for the four incident energies. This corresponds to $N/Z=1.39$ that is the same ratio as the initial system.

This choice is justified by some dynamical calculations of source parameters in this energy range [45,46]. Although the N/Z ratio of the SMM primary fragments increases slightly with increasing Z of the fragments, it remains very close to the N/Z ratio of the initial source [47]. Therefore, we will compare the results of these calculations to the extracted experimental results using the N/Z conservation hypothesis. The freeze-out volume has been fixed to three times the normal volume. Finally, for each incident energy, we used the excitation energy of the initial source as a free parameter. The thermal excitation energy values that reproduce best the charge distributions of the detected fragments are given in Table II.

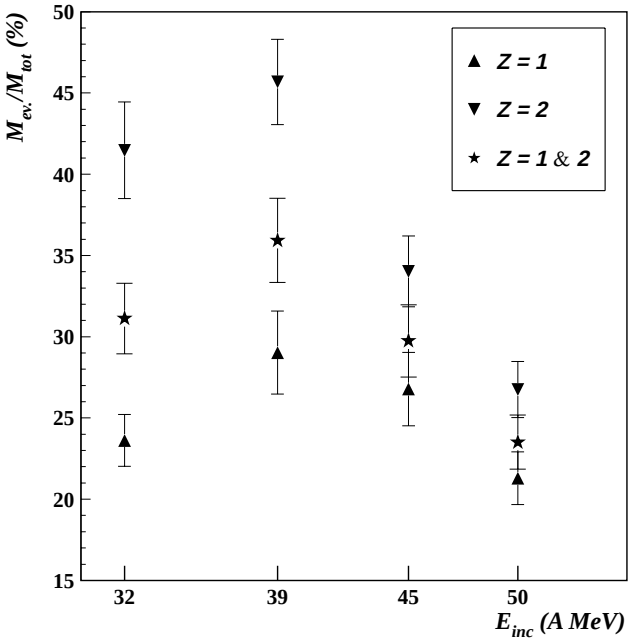

FIG. 15. The ratios of the multiplicities per event of the secondary particles evaporated by the primary fragments to the total emitted LCP vs the beam energy for the Xe+Sn central collisions.

A. Characteristics of the primary fragments

We have used a version of SMM, where we have access to the freeze-out configuration, i.e., to primary fragments' characteristics before secondary decay and Coulomb propagation. This standard version is described in Ref. [14].

The results of the SMM calculation, extracted directly from the freeze-out volume, are compared to the data in Fig. 16. The excitation energy of the primary fragments are globally well reproduced for the four incident energies.

Small deviations are, however, observed for large primary fragment charges in particular for the 32*A* MeV case. The experimental saturation of the excitation energy is not reproduced.

TABLE II. Thermal excitation energies in *A* MeV used in SMM simulations. Experimental and calculated average excitation energies of the primary fragments produced in central collisions of Xe +Sn at four incident energies.

Beam energy (*A* MeV)	32	39	45	50
Thermal excitation energy	5.	6.	6.5	7.
$\langle E^*/A\rangle_{exp.}$ (MeV)	2.26	3.02	3.26	3.13
$\langle E^*/A\rangle_{SMM}$ (MeV)	2.97	3.26	3.39	3.55

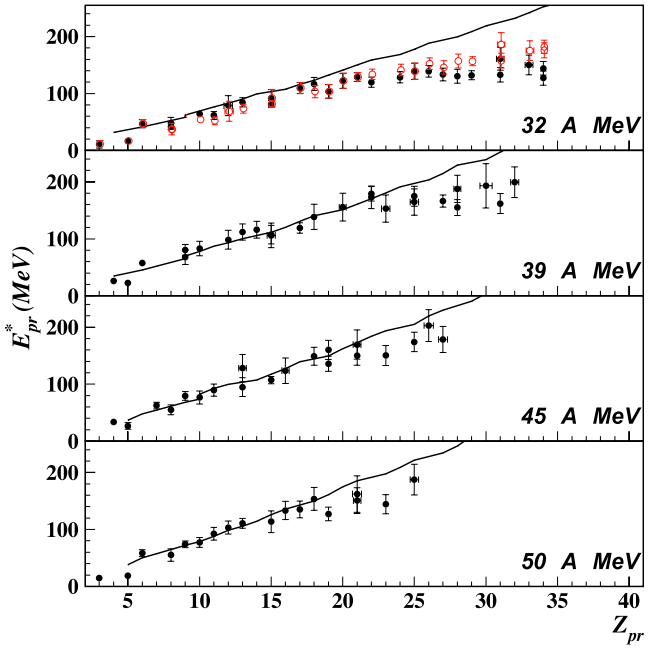

FIG. 16. Average excitation energy of the primary fragments as a function of their atomic number for the central collisions of Xe + Sn at 32, 39, 45, and 50 *A* MeV. The primary fragments are assumed to have same N/Z ratio as the combined system. The symbols present the data and curves SMM calculation. The masses of detected fragments are assumed to follow the valley of stability except for the data points represented by open circles where the EAL assumption is used (see text).

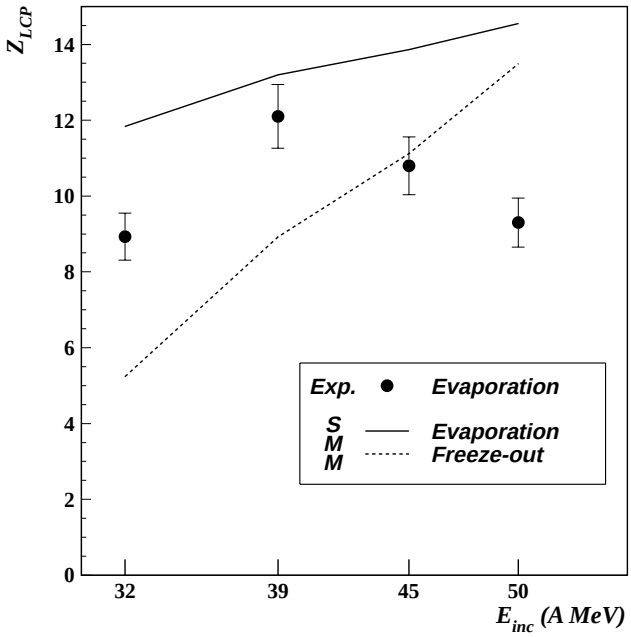

FIG. 17. Total charge contributions of secondary evaporated particles and LCP produced at the freeze-out as a function of the beam energy. The symbols represent the central collisions of Xe + Sn data, evaporative part of SMM calculations is presented by histogram and the freeze-out contribution by the dotted histogram.

Quantitative comparisons with the experimental excitation energy per nucleon averaged over the charge range of the measured fragments, are presented in Table II. The values of the calculated $\langle e^*_{pr} \rangle$ show smooth increase with the beam energy, while the data seems to saturate at 3*A* MeV above 39*A* MeV.

B. Evaporated light charged particles

The contribution of the secondary evaporated LCP reflects the excitation energy of the primary fragments discussed in the previous paragraph. How do the small differences between the data and the calculation for the excitation energy affect the predicted LCP multiplicities? We compare in Fig. 17 the charge contribution of total evaporated LCP resulting from SMM to the data.

The values extracted from the calculation are of the same order of magnitude as the experimental ones. However, the trend is not reproduced, SMM overestimates the evaporative contribution.

At 32*A* MeV, the discrepancy can be due to the limited charge range considered experimentally. Indeed, due to low statistics as we already mentioned, we do not take into account evaporation from heavier fragments, which are however, more excited than lighter ones. To check this point, we extracted the total evaporated particles by using the correlation functions of reduced velocities instead of the relative velocities ($V_{red} = V_{rel}/\sqrt{Z1+Z2}$). This variable has the advantage to eliminate the charge dependence of the fragment-LCP relative velocity correlation functions [48]. Following this procedure, taking all fragments into account, the total charge of evaporated particles increases significantly to be in agreement with the calculated value for the 32*A* MeV case.

For the 50*A* MeV case, where the limitation in the charge range is more important than for the other beam energies, the evaporated contribution changes very little and fails to increase the value of total evaporated charge from $Z_{LCP}=9$ to $Z_{LCP}=14$ predicted by SMM (Fig. 17).

The discrepancy is real, though, partly, it is caused by the thermal source size, which should decrease with the beam energy. The SMM calculations do predict the decrease of the number of evaporated LCP, because of decreasing size and number of IMF at very large excitation energies, in the ''falling'' part of the ''rise and fall'' of multifragmentation. However, in the experiment, this effect is observed when the maximum of multifragmentation is not yet reached. In the calculations, this behavior takes place because the number of evaporated α particles increases, contrary to the experimental result. This could be a consequence of the secondary deexcitation prescription employed in SMM [42]. An other possible reason would be an overexcitation of light primary IMF's predicted by SMM. The decay of these IMF's contributes considerably into LCP production and their share increases with the thermal energy.

The decrease of the experimental evaporated component Z_{LCP} at high energy could be alternatively understood if we consider the increasing effect of the collision dynamics. The direct emission of LCP increases with the incident energy, while the proportion of the thermal contribution decreases. This could be mocked up in the SMM calculations by de-

creasing the thermal source size, but can in no case be predicted by SMM.

It is worth noting the contribution of light charged particles produced at freeze-out as predicted by SMM. Figure 17 shows that this contribution increases with the beam energy more rapidly than that of the evaporated particles.

VI. DISCUSSION OF RESULTS

In this work, we have directly measured the saturation of the thermal excitation energy deposited in fragments produced in central heavy-ion collisions between 32 and 50 *A* MeV, by associating with each detected cold fragment the light charged particles evaporated by the primary excited parent nucleus. This saturation at excitation energies of around 3*A* MeV observed in Sec. III (see Fig. 14) is accompanied by a saturation of the number of evaporated LCP, that leads to a decrease in the proportion of evaporated to all detected LCP, with increasing incident energy (see Fig. 15 or Fig. 17). It should be recalled that the decrease of fragment excited state lifetimes with the excitation energy can limit the mean excitation values obtained in this paper. However, simulations we have performed indicate that the effect of shorter lifetimes on the efficiency of the method is quite small for primary fragment excitation energies up to 7.5*A* MeV.

A similar saturation has been observed in an earlier work by Jiang *et al.* [49] using a completely different experimental method, based on the measurement of neutron multiplicities. The authors claimed the saturation of the thermal energy deposited in hot nuclei formed in collisions of Ar + Au and Ar + Th in the energy range 27–77 *A* MeV. Their claim was based on the observation of a saturation of the multiplicity of evaporated neutrons, as well as that of the light charged particles detected in coincidence at backward angles, in central collisions at increasing beam energies. The neutron multiplicity saturates for the system Ar + Th around 30*A* MeV at $\langle M_n \rangle = 35$. Let us note in passing that we estimate the neutron multiplicity per event evaporated by the system Xe + Sn to be $\langle M_n \rangle = 23$ at 39*A* MeV.

In Ref. [49], the authors concluded that the observed saturation was due to the increasing inefficiency of the reaction mechanism to deposit thermal energy in to the hot nuclei it produced, rather than it being related to reaching the limits of excitation energy or temperature that a nucleus may support. In the present work, the situation is complicated by the fact that we are dealing with several heated nuclei per event which may themselves result from the break up of some other heavy, hot system. However, the comparisons we performed with the SMM model may give us some clue to understand what is happening.

In this model, the statistical break up of a thermally equilibrated hot nuclear system into fragments and light particles is calculated. The mass, charge, and excitation energy used as input parameters for the model are assumed to represent a hot residue remaining after the far-from-equilibrium initial stages of the reaction. The thermalized excitation energy required for SMM to reproduce the charge distributions and excitation energies of primary fragments was found to increase only slightly with bombarding energy, from 5*A* MeV for the 32*A* MeV case to 7*A* MeV for the 50*A* MeV data (see Table II). This increase of 2*A* MeV in the amount of thermalized excitation energy is only 50% of the total available energy increase. The missing energy can clearly be seen in the failure of SMM to reproduce fragment kinetic energies. One way to remedy this problem is to suppose the onset of radial flow of the fragmenting system, then part of the increase in incident energy is retrieved as kinetic energy of fragments [30,43]. Without knowing the precise dynamics of the reactions, the comparison of our data with SMM calculations indicates that although the mechanism of energy deposition becomes less efficient in this energy range, it does not saturate and hotter initial systems can be formed in collisions with increasing incident energy. Thus, within the SMM framework, the observed saturation of fragment excitation energies can not be entirely due to collision dynamics. Nevertheless, such a conclusion must be treated with caution: one of the basic assumptions of SMM is that the collision dynamics are irrelevant for the calculation of the fragment partitions, and so are ignored. One must then ask oneself what is the pertinence of any ''information'' on dynamics deduced from such a model. Further investigations are in progress using a dynamical calculation.

It is interesting to compare our results with a recent compilation of limiting temperatures extracted from different experimental measurements [50]. It suggests that T_{lim} decreases with increasing nuclear mass, in good agreement with calculations [51,52]. The primary fragments considered in the present work (Fig. 10) have, at the very most, masses $A = 80$, while most of them have masses in the region $A = 10$–50. The corresponding limiting temperature from Ref. [50] is $T_{lim} = 9$ MeV or $E^*/A = 7.5A$ MeV. As these values are much higher than the 3*A* MeV maximum excitation energy we find in our primary fragments, the observed saturation is not compatible with these fragments having reached their T_{lim}.

However, in the same compilation limiting excitation energies $\leqslant 3A$ MeV are found for the heaviest nuclei with masses in the $A = 150$–200 range. If we suppose, as in the SMM model, that fragments are produced by the break up of a heavy composite system formed in the reaction then it is possible that the observed saturation of primary fragment excitation energies is due to the initial systems, whose excitation energies vary from 5 to 7 *A* MeV, attaining their (mass dependent) T_{lim}. If so, then the primary fragment excitation energies reflect the limiting temperature of these systems.

VII. CONCLUSION

We have presented in this paper, the experimental results of the intrinsic properties of the fragments produced in the central collisions of Xe+ Sn from 32 to 50 *A* MeV bombarding energy. Quantitative experimental determination of the size and excitation energy of the primary fragments produced at such collisions before their decay are given for the four beam energies. The comparison of these extracted quantities with models provides a crucial test of some of their basic assumptions.

The experimental methods used in this work are based on the relative velocity correlation functions between the detected fragment and light charged particles. Thus, we have extracted the average multiplicity of the evaporated particles and their average kinetic energies in the center of mass of the fragments. These two variables have been used in order to reconstruct the average charge, mass, and excitation energy of the primary fragments.

Our results show that for a given beam energy, the excitation energy per nucleon is almost constant over the whole studied range of fragment charge. The statistical multifragmentation model reproduces very well the internal excitation energy of the primary fragments. The average value of this quantity increase from 2.3*A* MeV for a beam energy 32*A* MeV to saturate around 3*A* MeV for 39*A* MeV and above.

We also deduced the proportion of evaporated light charged particles per event, amounting to 30% of the total measured LCP for the 32*A* MeV reaction, increasing to 35% at 39*A* MeV and decreasing down to 23% for 50*A* MeV. Therefore, the majority of light charged particles are not evaporated by excited primary fragments in these reactions. Neither the absolute values of this proportion nor its evolution are reproduced by SMM calculations assuming a constant size for the multifragmenting system.

The comparison of data with SMM calculations indicates that although some saturation of the efficiency of very central heavy-ion collisions to form hot nuclear systems occurs in the bombarding energy range 32–50 *A* MeV, this is not sufficient to explain the observed saturation of primary fragment excitation energies. However, in order to fully understand the mechanism responsible for this saturation, it is necessary to compare the data with a full calculation of the reaction dynamics. This will be the subject of a forthcoming paper.

ACKNOWLEDGMENTS

We thank the staff of the GANIL Accelerator facility for their support during the experiment. This work was supported by Le Commissariat à l'Energie Atomique, Le Centre National de la Recherche Scientifique, Le Ministère de l'Education Nationale, and le Conseil Regional de Basse Normandie.

[1] J. Aichelin, Phys. Rep. **202**, 233 (1991).
[2] R. Nebauer and J. Aichelin, Nucl. Phys. **A650**, 65 (1999).
[3] R. Nebauer, *et al.*, INDRA Collaboration, Nucl. Phys. **A658**, 67 (1999).
[4] O. Tirel, Ph.D. thesis, Université de Caen, 1998, GANIL T 98 02
[5] D.H.E. Gross, Rep. Prog. Phys. **53**, 605 (1990).
[6] A. Ono, H. Horiuchi, T. Maruyama, and A. Ohnishi, Prog. Theor. Phys. **87**, 1185 (1992).
[7] A. Ono and H. Horiuchi, Phys. Rev. C **53**, 2958 (1996).
[8] A. Ono, Phys. Rev. C **59**, 853 (1999).
[9] P. Chomaz, M. Colonna, A. Guarnera, and J. Randrup, Phys. Rev. Lett. **73**, 3512 (1994).
[10] A. Guarnera, P. Chomaz, M. Colonna, and J. Randrup, Phys. Lett. B **403**, 191 (1997).
[11] S. Hudan, Ph.D. thesis, Université de Caen, 2001, GANIL T 01 07.
[12] S. Hudan *et al.* (unpublished).
[13] J.D. Frankland *et al.*, INDRA Collaboration, Nucl. Phys. **A689**, 940 (2001).
[14] J.P. Bondorf, A.S. Botvina, A.S. Iljinov, I.N. Mishustin, and K. Sneppen, Phys. Rep. **257**, 133 (1995).
[15] A.H. Raduta and A.R. Raduta, Phys. Rev. C **55**, 1344 (1997).
[16] A.H. Raduta and A.R. Raduta, Phys. Rev. C **56**, 2059 (1997).
[17] D.R. Dean and U. Mosel, Z. Phys. A **322**, 647 (1985).
[18] S. Levit and P. Bonche, Nucl. Phys. **A437**, 426 (1985).
[19] S.E. Koonin and J. Randrup, Nucl. Phys. **A474**, 173 (1987).
[20] N. Marie *et al.*, INDRA Collaboration, Phys. Rev. C **58**, 256 (1998).
[21] P. Staszel *et al.*, Phys. Rev. C **63**, 064610 (2001).
[22] J. Pouthas *et al.*, Nucl. Instrum. Methods Phys. Res. A **357**, 418 (1995).
[23] J.C. Steckmeyer *et al.*, Nucl. Instrum. Methods Phys. Res. A **361**, 472 (1995).
[24] J. Pouthas *et al.*, Nucl. Instrum. Methods Phys. Res. A **369**, 222 (1995).
[25] G. Tăbăcaru *et al.*, INDRA Collaboration, Nucl. Instrum. Methods Phys. Res. A **428**, 379 (1999).
[26] M. Pârlog *et al.*, INDRA Collaboration, Nucl. Instrum. Methods Phys. Res. A **482**, 674 (2002).
[27] M. Pârlog *et al.*, INDRA Collaboration, Nucl. Instrum. Methods Phys. Res. A **482**, 693 (2002).
[28] J. Lecolley *et al.*, Phys. Lett. B **391**, 317 (1994).
[29] J. Cugnon and D. L'Hote, Nucl. Phys. **A397**, 519 (1983).
[30] N. Marie *et al.*, INDRA Collaboration, Phys. Lett. B **391**, 15 (1997).
[31] J.D. Frankland *et al.*, INDRA Collaboration, Nucl. Phys. **A689**, 905 (2001).
[32] S. Salou, Ph.D. thesis, Université de Caen, 1997, GANIL T 97 06.
[33] S. Hudan *et al.*, INDRA Collaboration, in *Proceedings of the XXXVIII International Winter Meeting on Nuclear Physics*, edited by I. Iori (Ricerca Scientifica ed Educazione Permanente, Milano, Italy, 2000).
[34] D. Drijard, H.G. Fischer, and T. Nakada, Nucl. Instrum. Methods Phys. Res. A **225**, 367 (1984).
[35] D. Durand *et al.*, Nucl. Phys. **A541**, 266 (1992).
[36] A. Bonasera *et al.*, Phys. Rep. **243**, 1 (1994).
[37] R.J. Charity, Phys. Rev. C **58**, 1073 (1998).
[38] R.J. Charity *et al.*, Nucl. Phys. **A483**, 371 (1988).
[39] T. Nayak *et al.*, Phys. Rev. C **45**, 132 (1992).
[40] A.S. Parvan, V.D. Toneev, and K.K. Gudima, Phys. At. Nucl. **62**, 1497 (1999).
[41] S. Pratt and S. Das Gupta, Phys. Rev. C **62**, 044603 (2000).
[42] A. Botvina *et al.*, Nucl. Phys. **A475**, 663 (1987).
[43] R. Bougault *et al.*, INDRA Collaboration, in *Proceedings of the XXXV International Winter Meeting on Nuclear Physics*, edited by I. Iori (Ricerca Scientifica ed Educazione Permanente, Milano, Italy, 1997).
[44] N. Leneindre, Ph.D. thesis, Université de Caen, 1999.

[45] A.S. Botvina *et al.*, Phys. At. Nucl. **58**, 1703 (1995).
[46] W.P. Tan *et al.*, Phys. Rev. C **64**, 051901(R) (2001).
[47] A.S. Botvina and I.N. Mishustin, Phys. Rev. C **63**, 061601(R) (2001).
[48] Y. Kim *et al.*, Phys. Rev. C **45**, 387 (1992).
[49] D. Jiang *et al.*, Nucl. Phys. **A503**, 560 (1989).
[50] J. Natowitz *et al.*, Phys. Rev. C **65**, 034618 (2002).
[51] Y. Zhang *et al.*, Phys. Rev. C **54**, 1137 (1996).
[52] Y. Zhang *et al.*, Phys. Rev. C **59**, 3292 (1999).